LETTER

Direct detection of a break in the teraelectronvolt cosmic–ray spectrum of electrons and positrons

DAMPE Collaboration*

High-energy cosmic-ray electrons and positrons (CREs), which lose energy quickly during their propagation, provide a probe of Galactic high-energy processes[1–7] and may enable the observation of phenomena such as dark-matter particle annihilation or decay[8–10]. The CRE spectrum has been measured directly up to approximately 2 teraelectronvolts in previous balloon- or space-borne experiments[11–16], and indirectly up to approximately 5 teraelectronvolts using ground-based Cherenkov γ-ray telescope arrays[17,18]. Evidence for a spectral break in the teraelectronvolt energy range has been provided by indirect measurements[17,18], although the results were qualified by sizeable systematic uncertainties. Here we report a direct measurement of CREs in the energy range 25 gigaelectronvolts to 4.6 teraelectronvolts by the Dark Matter Particle Explorer (DAMPE)[19] with unprecedentedly high energy resolution and low background. The largest part of the spectrum can be well fitted by a 'smoothly broken power-law' model rather than a single power-law model. The direct detection of a spectral break at about 0.9 teraelectronvolts confirms the evidence found by previous indirect measurements[17,18], clarifies the behaviour of the CRE spectrum at energies above 1 teraelectronvolt and sheds light on the physical origin of the sub-teraelectronvolt CREs.

The Dark Matter Particle Explorer (DAMPE; also known as 'Wukong' in China), which was launched into a Sun-synchronous orbit at an altitude of about 500 km on 17 December 2015, is a high-energy particle detector optimized for studies of CREs and γ-rays up to about 10 TeV. The DAMPE instrument, from top to bottom, consists of a plastic scintillator detector, a silicon–tungsten tracker-converter detector, a bismuth germanium oxide (BGO) imaging calorimeter, and a neutron detector[19]. The plastic scintillator detector measures the charge of incident particles with a high nuclear resolution up to atomic number $Z = 28$, and aids in the discrimination between photons and charged particles. The silicon–tungsten tracker-converter detector measures the charge and trajectory of charged particles, and reconstructs the direction of γ-rays converting into $e^+ e^-$ pairs. The BGO calorimeter[20], with a total depth of about 32 radiation lengths and about 1.6 nuclear interaction lengths, measures the energy of incident particles and provides efficient CRE identification. The neutron detector further improves the electron/proton discrimination at teraelectronvolt energies[19]. With the combination of these four sub-detectors, DAMPE has achieved effective rejection of the hadronic cosmic-ray background and much improved energy resolution for CRE measurements[19]. In 2014 and 2015 the DAMPE engineering qualification model (see Methods) was extensively tested using test beams at the European Organization for Nuclear Research (CERN). The test beam data demonstrated excellent energy resolution for electrons and γ-rays (better than 1.2% for energies[21,22] exceeding 100 GeV), and verified that the electron/proton discrimination capabilities of the system[19] are consistent with the simulation results.

The cosmic-ray proton-to-electron flux ratio increases from approximately 300 at 100 GeV to approximately 800 at 1 TeV. A robust electron/proton discrimination and an accurate estimate of the residual proton background are therefore crucial for reliable measurement of the CRE spectrum. As the major instrument onboard DAMPE, the BGO calorimeter ensures a well contained development of electromagnetic showers in the energy range of interest. The electron/proton discrimination method relies on an image-based pattern recognition, as adopted in the ATIC experiment[23]. It exploits the topological differences of the shower shape between hadronic and electromagnetic particles in the BGO calorimeter. This method, together with the event pre-selection procedure, is found to be able to reject >99.99% of the protons while keeping 90% of the electrons and positrons. The details of electron identification are presented in Methods (for example, in Extended Data Fig. 1 we show the consistency of the electron/proton discrimination between the flight data and the Monte Carlo simulations). Figure 1 illustrates the discrimination power of DAMPE between electrons and protons with deposited energies of 500–1,000 GeV, using the BGO images only.

The results reported in this work are based on data recorded between 27 December 2015 and 8 June 2017. Data collected while the satellite was passing the South Atlantic Anomaly has been excluded from the analysis. During these approximately 530 days of operation, DAMPE recorded more than 2.8 billion cosmic-ray events, including around 1.5 million CREs above 25 GeV. Figure 2 shows the corresponding CRE spectrum measured from the DAMPE data (see Table 1 for more details), compared with previously published results from the space-borne experiments AMS-02[14] and Fermi-LAT[16], as well as the ground-based experiment of the H.E.S.S. Collaboration[17,18]. The contamination
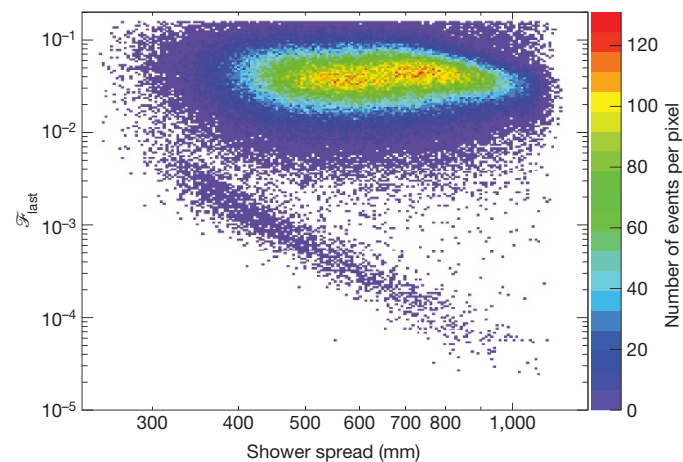

Figure 1 | Discrimination between electrons and protons in the BGO instrument of DAMPE. Both the electron candidates (the lower population) and proton candidates (the upper population) are for the DAMPE flight data with energies between 500 GeV and 1 TeV deposited in the BGO calorimeter. $\mathcal{F}_{last}$ represents the ratio of energy deposited in the last BGO layer to the total energy deposited in the BGO calorimeter[23]. The shower spread is defined as the summation of the energy-weighted shower dispersion of each layer.

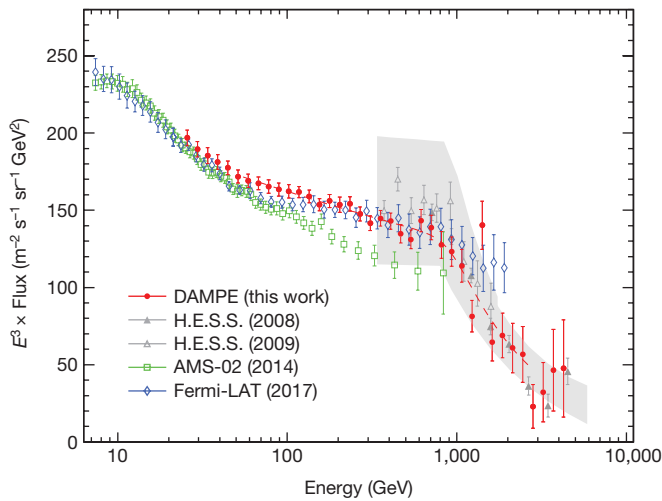*A list of authors and affiliations appears at the end of the paper.

Figure 2 | The CRE spectrum (multiplied by E^3) measured by DAMPE.
The red dashed line represents a smoothly broken power-law model that
best fits the DAMPE data in the range 55 GeV to 2.63 TeV. Also shown are
the direct measurements from the space-borne experiments AMS-02[14]
and Fermi-LAT[16], and the indirect measurement by the H.E.S.S.
Collaboration (the grey band represents its systematic errors apart from
the approximately 15% energy scale uncertainty)[17,18]. The error bars
($\pm 1\sigma$) of DAMPE, AMS-02 and Fermi-LAT include both systematic and
statistical uncertainties added in quadrature.

of the proton background for DAMPE is estimated to be less than 3% in
the energy range 50 GeV to 1 TeV (see Table 1). The systematic uncer-
tainties of the flux measurement have been evaluated, with dominant
contributions from the background subtraction and the instrumental
effective acceptance (the product of the fiducial instrumental acceptance
and the particle selection efficiency). More details on the systematic
uncertainties can be found in Methods.

A spectral hardening at about 50 GeV is shown in our data, in agree-
ment with that of AMS-02[14] and Fermi-LAT[16]. The data in the energy
range 55 GeV to 2.63 TeV fit much better to a smoothly broken power-
law model (the fit yields $\chi^2 = 23.3$ for 18 degrees of freedom) than to
a single power-law model (which yields $\chi^2 = 70.2$ for 20 degrees of
freedom). Our direct detection of a spectral break at $E \approx 0.9$ TeV, with
the spectral index changing from $\gamma_1 \approx 3.1$ to $\gamma_2 \approx 3.9$ (see Methods for
details), confirms the previous evidence found by the ground-based
indirect measurement of the H.E.S.S. Collaboration[17,18]. The AMS-02
data also predict a teraelectronvolt spectral softening with the so-called
minimal model[24]. Our results are consistent with the latest CRE spectra
measured by Fermi-LAT[16] in a wide energy range, although the tera-
electronvolt break has not been detected by Fermi-LAT, possibly
owing to higher particle background contamination and/or lower
instrumental energy resolution. We note that the CRE flux measured
by DAMPE is overall higher than the one reported by AMS-02 for
energies exceeding 70 GeV. The difference might be due in part to the
uncertainty in the absolute energy scale, which would coherently shift
the CRE spectrum up or down. With increased statistics and improved
understanding of the detector's performance, more consistent measure-
ments among different experiments may be achieved in the near future.

Table 1 | The CRE flux (in units of $m^{-2}\,s^{-1}\,sr^{-1}\,GeV^{-1}$) with 1σ statistical and systematic errors

Energy range (GeV)	$\langle E \rangle$ (GeV)	Acceptance ($m^2 \times sr$)	Counts	Background fraction	$\Phi\,(e^+ + e^-) \pm \sigma_{stat} \pm \sigma_{sys}$
24.0–27.5	25.7 ± 0.3	0.256 ± 0.007	377,469	(2.6 ± 0.3)%	(1.16 ± 0.00 ± 0.03) × 10⁻²
27.5–31.6	29.5 ± 0.4	0.259 ± 0.007	279,458	(2.5 ± 0.3)%	(7.38 ± 0.02 ± 0.19) × 10⁻³
31.6–36.3	33.9 ± 0.4	0.261 ± 0.007	208,809	(2.4 ± 0.2)%	(4.76 ± 0.02 ± 0.13) × 10⁻³
36.3–41.7	38.9 ± 0.5	0.264 ± 0.007	156,489	(2.4 ± 0.2)%	(3.08 ± 0.01 ± 0.08) × 10⁻³
41.7–47.9	44.6 ± 0.6	0.266 ± 0.007	117,246	(2.3 ± 0.2)%	(2.00 ± 0.01 ± 0.05) × 10⁻³
47.9–55.0	51.2 ± 0.6	0.269 ± 0.007	87,259	(2.3 ± 0.2)%	(1.28 ± 0.01 ± 0.03) × 10⁻³
55.0–63.1	58.8 ± 0.7	0.272 ± 0.007	65,860	(2.2 ± 0.2)%	(8.32 ± 0.04 ± 0.21) × 10⁻⁴
63.1–72.4	67.6 ± 0.8	0.275 ± 0.007	49,600	(2.1 ± 0.2)%	(5.42 ± 0.03 ± 0.13) × 10⁻⁴
72.4–83.2	77.6 ± 1.0	0.277 ± 0.007	37,522	(2.1 ± 0.2)%	(3.54 ± 0.02 ± 0.09) × 10⁻⁴
83.2–95.5	89.1 ± 1.1	0.279 ± 0.007	28,325	(2.1 ± 0.1)%	(2.31 ± 0.01 ± 0.06) × 10⁻⁴
95.5–109.7	102.2 ± 1.3	0.283 ± 0.007	21,644	(2.0 ± 0.1)%	(1.52 ± 0.01 ± 0.04) × 10⁻⁴
109.7–125.9	117.4 ± 1.5	0.282 ± 0.007	16,319	(2.0 ± 0.1)%	(1.00 ± 0.01 ± 0.02) × 10⁻⁴
125.9–144.5	134.8 ± 1.7	0.286 ± 0.007	12,337	(2.0 ± 0.1)%	(6.49 ± 0.06 ± 0.16) × 10⁻⁵
144.5–166.0	154.8 ± 1.9	0.287 ± 0.007	9,079	(2.0 ± 0.1)%	(4.14 ± 0.04 ± 0.10) × 10⁻⁵
166.0–190.6	177.7 ± 2.2	0.288 ± 0.007	7,007	(1.9 ± 0.1)%	(2.78 ± 0.03 ± 0.07) × 10⁻⁵
190.6–218.8	204.0 ± 2.6	0.288 ± 0.007	5,256	(2.0 ± 0.1)%	(1.81 ± 0.03 ± 0.05) × 10⁻⁵
218.8–251.2	234.2 ± 2.9	0.290 ± 0.007	4,002	(1.9 ± 0.1)%	(1.20 ± 0.02 ± 0.03) × 10⁻⁵
251.2–288.4	268.9 ± 3.4	0.291 ± 0.007	2,926	(2.0 ± 0.2)%	(7.59 ± 0.14 ± 0.19) × 10⁻⁶
288.4–331.1	308.8 ± 3.9	0.291 ± 0.007	2,136	(2.1 ± 0.2)%	(4.81 ± 0.11 ± 0.12) × 10⁻⁶
331.1–380.2	354.5 ± 4.4	0.290 ± 0.007	1,648	(2.1 ± 0.2)%	(3.25 ± 0.08 ± 0.08) × 10⁻⁶
380.2–436.5	407.1 ± 5.1	0.292 ± 0.007	1,240	(2.0 ± 0.2)%	(2.12 ± 0.06 ± 0.05) × 10⁻⁶
436.5–501.2	467.4 ± 5.8	0.291 ± 0.007	889	(2.2 ± 0.2)%	(1.32 ± 0.05 ± 0.03) × 10⁻⁶
501.2–575.4	536.6 ± 6.7	0.289 ± 0.007	650	(2.2 ± 0.2)%	(8.49 ± 0.34 ± 0.21) × 10⁻⁷
575.4–660.7	616.1 ± 7.7	0.288 ± 0.007	536	(2.0 ± 0.2)%	(6.13 ± 0.27 ± 0.15) × 10⁻⁷
660.7–758.6	707.4 ± 8.8	0.285 ± 0.007	390	(2.0 ± 0.2)%	(3.92 ± 0.20 ± 0.10) × 10⁻⁷
758.6–871.0	812.2 ± 10.2	0.284 ± 0.007	271	(2.3 ± 0.3)%	(2.38 ± 0.15 ± 0.06) × 10⁻⁷
871.0–1,000.0	932.5 ± 11.7	0.278 ± 0.008	195	(2.3 ± 0.3)%	(1.52 ± 0.11 ± 0.04) × 10⁻⁷
1,000.0–1,148.2	1,070.7 ± 13.4	0.276 ± 0.008	136	(2.6 ± 0.4)%	(9.29 ± 0.82 ± 0.27) × 10⁻⁸
1,148.2–1,318.3	1,229.3 ± 15.4	0.274 ± 0.009	74	(3.6 ± 0.5)%	(4.38 ± 0.53 ± 0.14) × 10⁻⁸
1,318.3–1,513.6	1,411.4 ± 17.6	0.267 ± 0.009	93	(2.2 ± 0.4)%	(4.99 ± 0.53 ± 0.17) × 10⁻⁸
1,513.6–1,737.8	1,620.5 ± 20.3	0.263 ± 0.010	33	(5.0 ± 0.9)%	(1.52 ± 0.28 ± 0.06) × 10⁻⁸
1,737.8–1,995.3	1,860.6 ± 23.3	0.255 ± 0.011	26	(5.4 ± 0.9)%	(1.07 ± 0.22 ± 0.05) × 10⁻⁸
1,995.3–2,290.9	2,136.3 ± 26.7	0.249 ± 0.012	17	(5.8 ± 0.9)%	(6.24 ± 1.61 ± 0.30) × 10⁻⁹
2,290.9–2,630.3	2,452.8 ± 30.7	0.243 ± 0.014	12	(7.9 ± 1.1)%	(3.84 ± 1.20 ± 0.21) × 10⁻⁹
2,630.3–3,019.9	2,816.1 ± 35.2	0.233 ± 0.015	4	(18.2 ± 2.5)%	(1.03 ± 0.63 ± 0.07) × 10⁻⁹
3,019.9–3,467.4	3,233.4 ± 40.4	0.227 ± 0.017	4	(15.4 ± 2.4)%	(9.53 ± 5.64 ± 0.70) × 10⁻¹⁰
3,467.4–3,981.1	3,712.4 ± 46.4	0.218 ± 0.018	4	(11.2 ± 2.6)%	(9.07 ± 5.12 ± 0.77) × 10⁻¹⁰
3,981.1–4,570.9	4,262.4 ± 53.3	0.210 ± 0.020	3	(11.4 ± 4.0)%	(6.15 ± 4.02 ± 0.60) × 10⁻¹⁰

$\langle E \rangle$ is the representative value of the energy in the bin, calculated in the same way as in ref. 14.

Unlike the H.E.S.S. data, which are dominated by systematic uncertainties, the DAMPE CRE spectrum shown in Fig. 2 is dominated by statistical uncertainties for energies above about 380 GeV. DAMPE is designed to operate for at least three years, and will probably be extended to a longer lifetime given the current instrument status. Further statistics will allow more precise measurement of the CRE spectrum up to higher energies of about 10 TeV and, crucially, test whether there is any edge-like feature that may be generated by dark-matter annihilation or decay or nearby pulsars[4,7,25]. The precise measurement of the CRE spectrum by DAMPE can narrow down the parameter space of models, such as those containing nearby pulsars, supernova remnants and candidates of particle dark matter, considerably[3,26–29] in order to account for the "positron anomaly"[24,30]. The parameters include, for example, the spectral cutoff energy of the electrons accelerated by nearby pulsars or supernova remnants, or the rest mass and the annihilation cross-section (or alternatively the lifetime) of a dark-matter particle. Together with data from the cosmic microwave background or γ-rays, these improved constraints on the model parameters obtained by DAMPE may clarify the connection between the positron anomaly and the annihilation or decay of particle dark matter.

Online Content Methods, along with any additional Extended Data display items and Source Data, are available in the online version of the paper; references unique to these sections appear only in the online paper.

1. Meyer, P. Cosmic rays in the Galaxy. *Annu. Rev. Astron. Astrophys.* **7,** 1–38 (1969).
2. Strong, A. W., Moskalenko, I. V. & Ptuskin, V. S. Cosmic-ray propagation and interactions in the Galaxy. *Annu. Rev. Nucl. Part. Sci.* **57,** 285–327 (2007).
3. Fan, Y. Z., Zhang, B. & Chang, J. Electron/positron excesses in the cosmic ray spectrum and possible interpretations. *Int. J. Mod. Phys. D* **19,** 2011–2058 (2010).
4. Shen, C. S. Pulsars and very high-energy cosmic-ray electrons. *Astrophys. J.* **162,** L181–L186 (1970).
5. Aharonian, F. A., Atoyan, A. M. & Voelk, H. J. High energy electrons and positrons in cosmic rays as an indicator of the existence of a nearby cosmic tevatron. *Astron. Astrophys.* **294,** L41–L44 (1995).
6. Moskalenko, I. V. & Strong, A. W. Production and propagation of cosmic-ray positrons and electrons. *Astrophys. J.* **493,** 694–707 (1998).
7. Kobayashi, T., Komori, Y., Yoshida, K. & Nishimura, J. The most likely sources of high-energy cosmic-ray electrons in supernova remnants. *Astrophys. J.* **601,** 340–351 (2004).
8. Turner, M. & Wilczek, F. Positron line radiation as a signature of particle dark matter in the halo. *Phys. Rev. D* **42,** 1001–1007 (1990).
9. Bertone, G., Hooper, D. & Silk, J. Particle dark matter: evidence, candidates and constraints. *Phys. Rep.* **405,** 279–390 (2005).
10. Feng, J. L. Dark matter candidates from particle physics and methods of detection. *Annu. Rev. Astron. Astrophys.* **48,** 495–545 (2010).
11. Nishimura, J. *et al.* Emulsion chamber observations of primary cosmic-ray electrons in the energy range 30–1000 GeV. *Astrophys. J.* **238,** 394–409 (1980).
12. Chang, J. *et al.* (The ATIC Collaboration) An excess of cosmic ray electrons at energies of 300–800 GeV. *Nature* **456,** 362–365 (2008).
13. Abdo, A. A. *et al.* (The Fermi-LAT Collaboration) Measurement of the cosmic ray $e^+ + e^-$ spectrum from 20 GeV to 1 TeV with the Fermi Large Area Telescope. *Phys. Rev. Lett.* **102,** 181101 (2009).
14. Aguilar, M. *et al.* (The AMS-02 Collaboration) Precision measurement of the $(e^+ + e^-)$ flux in primary cosmic rays from 0.5 GeV to 1 TeV with the Alpha Magnetic Spectrometer on the International Space Station. *Phys. Rev. Lett.* **113,** 221102 (2014).
15. Adriani, O. *et al.* (The PAMELA collaboration) Cosmic-ray electron flux measured by the PAMELA experiment between 1 and 625 GeV. *Phys. Rev. Lett.* **106,** 201101 (2011).
16. Abdollahi, S. *et al.* (The Fermi LAT Collaboration) Cosmic-ray electron+positron spectrum from 7 GeV to 2 TeV with the Fermi Large Area Telescope. *Phys. Rev. D* **95,** 082007 (2017).
17. Aharonian, F. *et al.* (The H.E.S.S. Collaboration) Energy spectrum of cosmic-ray electrons at TeV energies. *Phys. Rev. Lett.* **101,** 261104 (2008).
18. Aharonian, F. *et al.* (The H.E.S.S. Collaboration) Probing the ATIC peak in the cosmic-ray electron spectrum with H.E.S.S. *Astron. Astrophys.* **508,** 561–564 (2009).
19. Chang, J. *et al.* (The DAMPE collaboration) The Dark Matter Particle Explorer mission. *Astropart. Phys.* **95,** 6–24 (2017).
20. Zhang, Z. Y. *et al.* Design of a high dynamic range photomultiplier base board for the BGO ECAL of DAMPE. *Nucl. Instrum. Methods A* **780,** 21–26 (2015).
21. Yue, C. *et al.* A parameterized energy correction method for electromagnetic showers in BGO-ECAL of DAMPE. *Nucl. Instrum. Methods A* **856,** 11–16 (2017).
22. Zhang, Z. Y. *et al.* The calibration and electron energy reconstruction of the BGO ECAL of the DAMPE detector. *Nucl. Instrum. Methods A* **836,** 98–104 (2016).
23. Chang, J. *et al.* (The ATIC Collaboration) Resolving electrons from protons in ATIC. *Adv. Space Res.* **42,** 431–436 (2008).
24. Accardo, L. *et al.* (The AMS collaboration) High statistics measurement of the positron fraction in primary cosmic rays of 0.5–500 GeV with the Alpha Magnetic Spectrometer on the International Space Station. *Phys. Rev. Lett.* **113,** 121101 (2014).
25. Hooper, D., Cholis, I., Linden, T. & Fang, K. HAWC observations strongly favor pulsar interpretations of the cosmic-ray positron excess. *Phys. Rev. D* **96,** 103013 (2017).
26. Blasi, P. Origin of the positron excess in cosmic rays. *Phys. Rev. Lett.* **103,** 051104 (2009).
27. Hooper, D., Blasi, P. & Serpico, P. D. Pulsars as the sources of high energy cosmic ray positrons. *J. Cosmol. Astropart. Phys.* **0901,** 025 (2009).
28. Abdollahi, S. *et al.* (The Fermi-LAT Collaboration) Search for cosmic-ray electron and positron anisotropies with seven years of Fermi Large Area Telescope data. *Phys. Rev. Lett.* **118,** 091103 (2017).
29. Bergström, L., Edsjö, J. & Zaharijas, G. Dark matter interpretation of recent electron and positron data. *Phys. Rev. Lett.* **103,** 031103 (2009).
30. Adriani, O. *et al.* (The PAMELA Collaboration) An anomalous positron abundance in cosmic rays with energies 1.5–100 GeV. *Nature* **458,** 607–609 (2009).

Author Contributions This work is the result of the contributions and efforts of all the participating institutes, under the leadership of Purple Mountain Observatory, the Chinese Academy of Sciences. All authors have reviewed, discussed, and commented on the present results and on the manuscript. In line with collaboration policy, the authors are listed alphabetically.

DAMPE Collaboration

G. Ambrosi[1], Q. An[2,3], R. Asfandiyarov[4], P. Azzarello[4], P. Bernardini[5,6], B. Bertucci[1,7], M. S. Cai[8,9], J. Chang[8,9], D. Y. Chen[8,10], H. F. Chen[2,3], J. L. Chen[11], W. Chen[8,10], M. Y. Cui[8], T. S. Cui[12], A. D'Amone[5,6], A. De Benedittis[5,6], I. De Mitri[5,6], M. Di Santo[6], J. N. Dong[2,3], T. K. Dong[8], Y. F. Dong[13], Z. X. Dong[12], G. Donvito[14], D. Droz[4], K. K. Duan[8,10], J. L. Duan[11], M. Duranti[1,7], D. D'Urso[1,15], R. R. Fan[13], Y. Z. Fan[8,9], F. Fang[11], C. Q. Feng[2,3], L. Feng[8], P. Fusco[14,16], V. Gallo[4], F. J. Gan[2,3], M. Gao[13], S. S. Gao[2,3], F. Gargano[14], S. Garrappa[1,7], K. Gong[13], Y. Z. Gong[8], D. Y. Guo[13], J. H. Guo[8], Y. M. Hu[8], G. S. Huang[2,3], Y. Y. Huang[8], M. Ionica[1], D. Jiang[2,3], W. Jiang[8,9], X. Jin[2,3], J. Kong[11], S. J. Lei[8], S. Li[8,10], X. Li[8], W. L. Li[12], Y. Li[11], Y. F. Liang[8,10], Y. M. Liang[12], N. H. Liao[8], H. Liu[8], J. Liu[11], S. B. Liu[2,3], W. Q. Liu[11], Y. Liu[8], F. Loparco[14,16], M. Ma[12], P. X. Ma[8,9], S. Y. Ma[2,3], T. Ma[8], X. Q. Ma[12], X. Y. Ma[12], G. Marsella[5,6], M. N. Mazziotta[14], D. Mo[11], X. Y. Niu[11], X. Y. Peng[8], W. X. Peng[13], R. Qiao[13], J. N. Rao[12], M. M. Salinas[4], G. Z. Shang[12], W. H. Shen[12], Z. Q. Shen[8,10], Z. T. Shen[2,3], J. X. Song[12], H. Su[11], M. Su[8,17], Z. Y. Sun[11], A. Surdo[6], X. J. Teng[12], X. B. Tian[12], A. Tykhonov[4], V. Vagelli[1,7], S. Vitillo[4], C. Wang[2,3], H. Wang[12], H. Y. Wang[13], J. Z. Wang[13], L. G. Wang[12], Q. Wang[2,3], S. Wang[8,10], X. H. Wang[11], X. L. Wang[2,3], Y. F. Wang[2,3], Y. P. Wang[8,10], Y. Z. Wang[8,10], S. C. Wen[8,10], Z. M. Wang[11], D. M. Wei[8,9], J. J. Wei[8], Y. F. Wei[2,3], D. Wu[13], J. Wu[8,9], L. B. Wu[2,3], S. S. Wu[12], X. Wu[4], K. Xi[11], Z. Q. Xia[8,9], Y. L. Xin[8], H. T. Xu[12], Z. L. Xu[8,10], Z. Z. Xu[2,3], G. F. Xue[12], H. B. Yang[11], P. Yang[11], Y. Q. Yang[11], Z. L. Yang[11], H. J. Yao[11], Y. H. Yu[11], Q. Yuan[8,9], C. Yue[8,10], J. J. Zang[8], C. Zhang[8], D. L. Zhang[2,3], F. Zhang[13], J. B. Zhang[2,3], J. Y. Zhang[13], J. Z. Zhang[11], L. Zhang[8,10], P. F. Zhang[8], S. X. Zhang[11], W. Z. Zhang[12], Y. Zhang[8,10], Y. J. Zhang[11], Y. Q. Zhang[8,10], Y. L. Zhang[2,3], Y. P. Zhang[11], Z. Zhang[8], Z. Y. Zhang[2,3], H. Zhao[13], H. Y. Zhao[12], X. F. Zhao[12], C. Y. Zhou[12], Y. Zhou[11], X. Zhu[2,3], Y. Zhu[12] & S. Zimmer[4]

[1]Istituto Nazionale di Fisica Nucleare (INFN)—Sezione di Perugia, I-06123 Perugia, Italy. [2]State Key Laboratory of Particle Detection and Electronics, University of Science and Technology of China, Hefei 230026, China. [3]Department of Modern Physics, University of Science and Technology of China, Hefei 230026, China. [4]Department of Nuclear and Particle Physics, University of Geneva, CH-1211 Geneva, Switzerland. [5]Dipartimento di Matematica e Fisica E. De Giorgi, Università del Salento, I-73100 Lecce, Italy. [6]Istituto Nazionale di Fisica Nucleare (INFN)—Sezione di Lecce, I-73100 Lecce, Italy. [7]Dipartimento di Fisica e Geologia, Università degli Studi di Perugia, I-06123 Perugia, Italy. [8]Key Laboratory of Dark Matter and Space Astronomy, Purple Mountain Observatory, Chinese Academy of Sciences, Nanjing 210008, China. [9]School of Astronomy and Space Science, University of Science and Technology of China, Hefei 230026, China. [10]University of Chinese Academy of Sciences, Yuquan Road 19, Beijing 100049, China. [11]Institute of Modern Physics, Chinese Academy of Sciences, Nanchang Road 509, Lanzhou 730000, China. [12]National Space Science Center, Chinese Academy of Sciences, Nanertiao 1, Zhongguancun, Haidian district, Beijing 100190, China. [13]Institute of High Energy Physics, Chinese Academy of Sciences, YuquanLu 19B, Beijing 100049, China. [14]Istituto Nazionale di Fisica Nucleare (INFN)—Sezione di Bari, I-70125 Bari, Italy. [15]ASI Space Science Data Center (SSDC), I-00133 Roma, Italy. [16]Dipartimento di Fisica 'M. Merlin' dell'Univerisità e del Politecnico di Bari, I-70126 Bari, Italy. [17]Department of Physics and Laboratory for Space Research, University of Hong Kong, Pok Fu Lam, Hong Kong, China.

METHODS

Discrimination between electrons and protons. The method of electron selection in this work relies on the differences in the development of showers initiated by protons and electrons[23,31,32]. The procedure is as follows. First, we search for events passing through the entire BGO calorimeter. We select events with hit positions from −28.5 cm to 28.5 cm for the top layer and −28 cm to 28 cm for the bottom layer (each BGO bar lies between −30 cm and 30 cm). Second, we calculate the shower spread, expressed by the energy-weighted root-mean-square value of hit positions in the calorimeter. The root-mean-square value of the ith layer is calculated as:

$$\mathrm{RMS}_i = \sqrt{\frac{\sum_j (x_{j,i} - x_{c,i})^2 E_{j,i}}{\sum_j E_{j,i}}} \tag{1}$$

where $x_{j,i}$ and $E_{j,i}$ are the coordinates and deposited energy of the jth bar in the ith layer, and $x_{c,i}$ is the coordinate of the shower centre of the ith layer. Figure 1 shows the deposited energy fraction in the last BGO layer ($\mathcal{F}_{\mathrm{last}}$) versus the total root-mean-square value of all 14 BGO layers (that is, $\sum_i \mathrm{RMS}_i$). We can see that electrons are well separated from protons. Note that in Fig. 1 and Extended Data Fig. 1, heavy ions have already been effectively removed by selection through the plastic scintillator detector, on the basis of the charge measurement.

Extensive Monte Carlo simulations are carried out to compare with data. Our Monte Carlo simulations are based on Geant4.10.02[33]. The hadronic model QGSP_BERT is used to generate the proton sample used in this analysis. We have compared the two hadronic models in Geant4, QGSP_BERT and FTFP_BERT, for the high-energy range (>50 GeV), and found that the difference in the proton contamination estimates between the two models is less than 10% for energies up to 5 TeV. The corresponding systematic uncertainty on the CRE spectrum measurement is thus negligible.

For a better evaluation of the electron/proton discrimination capabilities, we introduce a dimensionless variable, ζ, defined as

$$\zeta = \mathcal{F}_{\mathrm{last}} \times (\Sigma_i \mathrm{RMS}_i / \mathrm{mm})^4 / (8 \times 10^6) \tag{2}$$

The ζ distribution for events with deposited energies from 500 GeV to 1 TeV in the BGO calorimeter is shown in Extended Data Fig. 1. Blue points represent the flight data, and the red histogram represents the Monte Carlo data (the electron Monte Carlo data are in black and the proton Monte Carlo data are in green). The Monte Carlo data and the flight data are in good agreement with each other. A clear separation between electrons and protons is shown. The electron/proton discrimination capability with the ζ variable has also been validated with the 400-GeV proton data collected at the CERN beam test facilities using the DAMPE engineering qualification model. The engineering qualification model is essentially the same as the final flight model, except that 166 out of the 192 silicon ladders in the silicon–tungsten tracker-converter detector are ladders equipped with non-segmented silicon detectors and without the readout application-specific integrated circuits, but otherwise have the same material, mechanical and thermal properties as the real ones[34]. In the data analysis, we take an upper bound of $\zeta \approx 8.5$ for the CRE candidates.

We also check the consistency of the ζ variable between the two-side readouts, the P (positive) and N (negative) sides, of the BGO crystal. The gains of the two sides differ by a factor of about 5. The data sets from each end can be used to measure the energy, and hence provide the particle identification, independently. The distribution of their ratio shows that the two groups of readout-based ζ values of the CRE candidates agree well with one another with no evidence of asymmetry between the P- and N-sides, as illustrated in Extended Data Fig. 2.

As independent analyses, principal component analysis[35] and boosted decision tree[36] classifiers have been adopted for electron/proton discrimination, which have discrimination powers similar to the ζ method. These three methods give very consistent (within the statistical uncertainties) results of the final CRE flux. In Fig. 2 we present the ζ-method-based spectrum.

Proton contamination estimate. The consistency between the Monte Carlo simulations and the flight data (see Extended Data Fig. 1) shows that we can use the simulation data as templates, which are normalized through fitting to the flight data, to estimate the proton contamination in the signal region. The contamination fraction is smaller than 6% for energies below approximately 2 TeV without substantial fluctuation. The estimated proton contamination has been subtracted in the final CRE spectrum shown in Fig. 2 and in the fluxes in Table 1.

Systematic uncertainties of the CRE flux measurement. We evaluated the systematic uncertainties of the flux measurement. The dominant sources are related to the background subtraction and the effective acceptance (the product of the geometrical acceptance and the selection efficiency). We evaluated the systematic effect of the proton contamination estimate by changing the modelling of ζ and the definition of the background region, taking into account also the limited

Monte Carlo statistics at high energy. The results are reported in Table 1 (that is, the background fraction).

The acceptance is determined by the BGO calorimeter. Since DAMPE has a precise tracking system, the reconstructed electron track can be used to define the incoming particle direction. The correlation between the track and the BGO shower direction is well reproduced by Monte Carlo simulation. We used the residual difference to estimate the systematic uncertainty by varying the geometrical acceptance cut, resulting in a 2.2% error that is independent of the particle energy.

For the selection efficiency, two components contribute the majority of the systematic uncertainties. One is the trigger efficiency. Its systematic uncertainty is evaluated by comparing the efficiency of the Monte Carlo simulation to the one measured from the pre-scaled data sample collected with lower trigger thresholds (the unbiased and low-energy triggers). The overall agreement is excellent and the difference is used to characterize the systematic uncertainty, giving 1.5% at 25 GeV and 1% at 2 TeV, respectively.

The other main systematic uncertainty arises from the selection of ζ. After subtracting the small number of proton candidates, the distribution of the ζ variable from the Monte Carlo simulation is in good agreement with the selected electron candidates from flight data. However, an energy-dependent difference between flight data and Monte Carlo simulation is observed, which is also confirmed by the 250-GeV electron data taken at the CERN beam test. The Monte Carlo ζ distribution is thus shifted to match the distribution of data, resulting in an efficiency correction of −1.9% at 25 GeV and 8.4% at 2 TeV, respectively. The systematic uncertainty of the CRE spectrum due to this correction is estimated to be 1.0% at 25 GeV and 4.2% at 2 TeV.

The absolute energy scale uncertainty constitutes another type of systematic uncertainty that will shift the spectrum up or down coherently, without changing the spectral features of the flux. For DAMPE, the absolute energy scale is estimated to be around 1.013 times higher[37]. Its small effect on the flux (that is, scaled down by a factor of around 2.6%) has not been corrected in this work.

Energy measurements. The BGO calorimeter is a total absorption electromagnetic calorimeter. Monte Carlo simulations show that the energy leakage from the bottom of the calorimeter is negligible even at teraelectronvolt energies because of the large thickness of the calorimeter (about 32 radiation lengths). Despite the energy loss in the dead material (such as the carbon fibre, used for support), more than 90% of the primary energy of an electron is deposited in the BGO crystals. An energy correction taking into account the incident position, direction and the shower development is applied to each electron candidate[21]. The beam-test data and the Monte Carlo simulations show that the energy resolution of DAMPE is better than 1.2% for electrons with energies[19] from 100 GeV to 10 TeV.
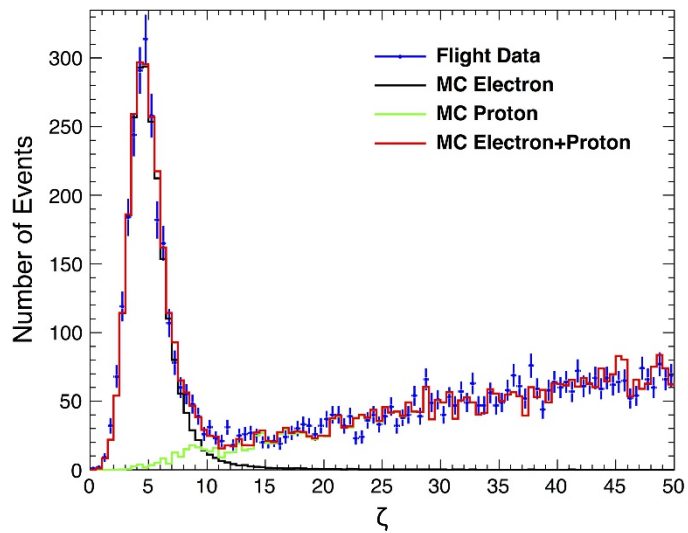
In addition, we checked the consistency of the energy ratio of each CRE candidate measured from the P- and N-sides. Extended Data Fig. 3 presents the ratios between the two sides, together with a Gaussian fit that gives a mean of 1.005 ± 0.005 and a σ of 0.016 ± 0.001, supporting the quoted energy resolution of about 1% from Monte Carlo simulations[19].

Comparison of different spectral models. We follow the procedures outlined in appendix C of ref. 16 to fit the CRE spectrum in the energy range 55 GeV to 2.63 TeV. The potential systematic uncertainties on the CRE flux measurement due to the ζ method (including the background contamination and the selection of ζ) is modelled by a set of nuisance correction parameters. The number of nuisance parameters is assumed to be $N = 6$, and the bin size was chosen to achieve equal-energy bins in logarithmic space. We fitted the data with a single power-law model ($\Phi = \Phi_0 (E/100\,\mathrm{GeV})^{-\gamma}$) and a smoothly broken power-law model ($\Phi = \Phi_0 (E/100\,\mathrm{GeV})^{-\gamma_1} [1 + (E/E_b)^{-(\gamma_1 - \gamma_2)/\Delta}]^{-\Delta}$ with the smoothness parameter[38] Δ fixed to be 0.1), respectively. The single-power-law fit yields $\Phi = (1.64 \pm 0.01) \times 10^{-4} (E/100\,\mathrm{GeV})^{-3.13 \pm 0.01}\,\mathrm{m}^{-2}\,\mathrm{s}^{-1}\,\mathrm{sr}^{-1}\,\mathrm{GeV}^{-1}$ with $\chi^2/\mathrm{d.o.f.} = 70.2/20$. The broken power-law fit yields $\gamma_1 = 3.09 \pm 0.01$, $\gamma_2 = 3.92 \pm 0.20$, $\Phi_0 = (1.62 \pm 0.01) \times 10^{-4}\,\mathrm{m}^{-2}\,\mathrm{s}^{-1}\,\mathrm{sr}^{-1}\,\mathrm{GeV}^{-1}$, $E_b = 914 \pm 98\,\mathrm{GeV}$ and $\chi^2/\mathrm{d.o.f.} = 23.3/18$. These fit results are shown in Extended Data Fig. 4. Compared with the single-power-law hypothesis, the χ^2 value is smaller by 46.9 for two fewer degrees of freedom in the smoothly broken power-law hypothesis. The smoothly broken power-law model is thus strongly preferred (at the 6.6σ level).
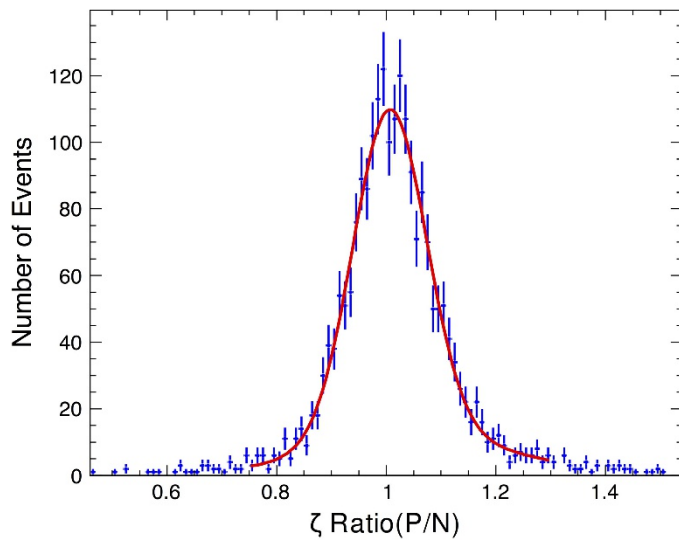
Code availability. The numerical code was developed specifically for the DAMPE data analysis. The uniqueness of the DAMPE design and the complexity involved in the data analysis means that the software package has limited application to the relevant community. We have opted not to make the code public.

Data availability. The cosmic-ray electron spectrum data, along with statistical and systematics uncertainties, are reported in Fig. 2 and available in Table 1. The other data that support the plots within this paper and other findings of this study are available from the DAMPE Collaboration (dampe@pmo.ac.cn) upon reasonable request.
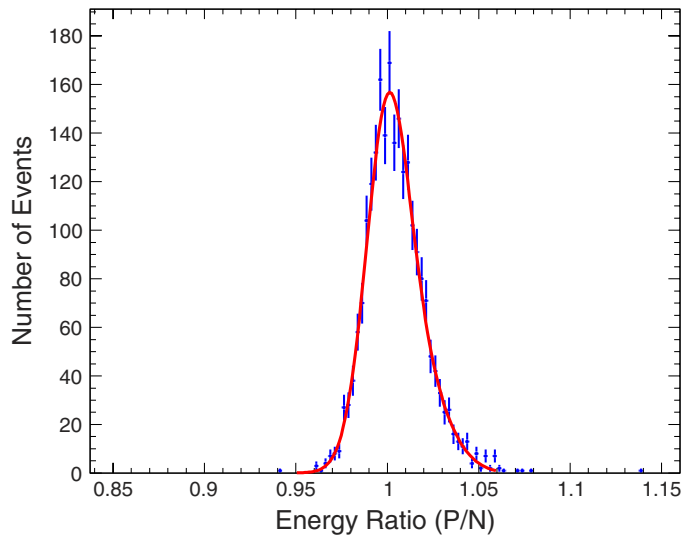
31. Chang, J. *et al.* On the detection and identification of cosmic gamma-rays in a cosmic ray detector. In *Proceedings of the 26th International Cosmic Ray Conference (Salt Lake City)* (eds Kieda, D. Salamon, M. & Dingus, B.) Vol. 5, 37 (1999); https://galprop.stanford.edu/elibrary/icrc/1999/proceedings/root/vol5/o4_1_10.pdf.

32. Schmidt, W. K. H. *et al.* On the identification of high energy cosmic ray electrons in the advanced thin ionization calorimeter (ATIC). In *Proceedings of the 26th International Cosmic Ray Conference (Salt Lake City)* (eds Kieda, D. Salamon, M. & Dingus, B.) Vol. 5, 41 (1999); https://galprop.stanford.edu/elibrary/icrc/1999/proceedings/root/vol5/o4_1_11.pdf.

33. Agostinelli, S. *et al.* Geant4—a simulation toolkit. *Nucl. Instrum. Methods A* **506,** 250–303 (2003).

34. Wu, X. *et al.* The Silicon-Tungsten Tracker of the DAMPE Mission. *Proc. Sci. (ICRC2015)* **1192** (2015); https://pos.sissa.it/236/1192/.

35. Jolliffe, I. T. *Principal Component Analysis* (Springer, 1986).

36. Roe, B. P. *et al.* Boosted decision trees as an alternative to artificial neural networks for particle identification. *Nucl. Instrum. Methods A* **543,** 577–584 (2005).

37. Zang, J. J. *et al.* Measurement of absolute energy scale of ECAL of DAMPE with geomagnetic rigidity cutoff. *Proc. Sci. (ICRC2017)* **197** (2017); https://pos.sissa.it/301/197/pdf.

38. Ackermann, M. *et al.* Detection of the characteristic pion-decay signature in supernova remnants. *Science* **339,** 807–811 (2013).
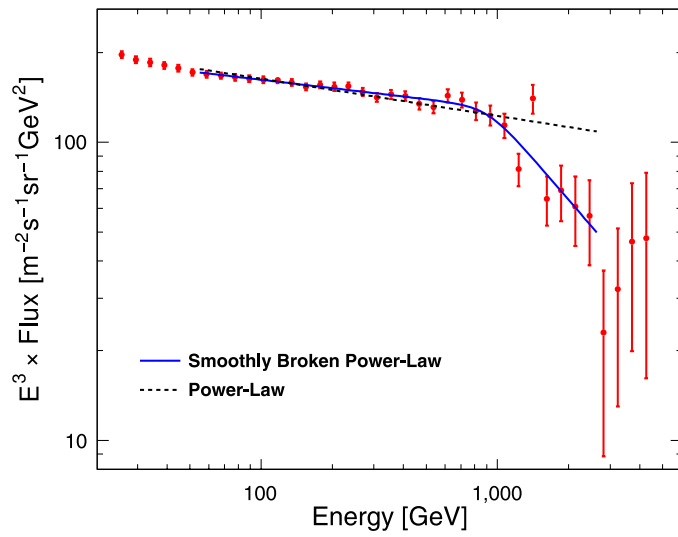
Extended Data Figure 1 | Comparison of the flight data and the Monte Carlo simulations of the ζ distributions. All events have deposited energies between 500 GeV and 1 TeV in the BGO calorimeter. The error bars ($\pm 1\sigma$) represent statistical uncertainties. As for the Monte Carlo (MC) simulation data, the black, green and red histograms represent the electrons, the protons and their sum, respectively.

Extended Data Figure 2 | Ratios of the ζ values calculated from the *P*- and *N*-side readout data. The events have deposited energies between 500 GeV and 1 TeV in the BGO calorimeter. The error bars ($\pm 1\sigma$) represent statistical uncertainties. The red line represents a Gaussian fit to the data points. The mean of the ratios is 1.015 ± 0.002 and σ is 0.110 ± 0.005.

Extended Data Figure 3 | Ratios of the energies reconstructed with the *P*- and *N*-side readout data. All events have deposited energies between 500 GeV and 1 TeV in the BGO calorimeter. The error bars (±1σ) represent statistical uncertainties. The red line represents a Gaussian fit to the data, with a mean of 1.005 ± 0.005 and a σ of 0.016 ± 0.001.

Extended Data Figure 4 | Comparison of two spectral models for the DAMPE CRE spectrum. The dashed and solid lines show the best-fitting results of the single power-law and smoothly broken power-law models, respectively.